CHAPTER 4

REDUCED GRAPHENE OXIDE-POLYPYRROLE NANOTUBES NANOCOMPOSITE ELECTRODE SYSTEM

This chapter deals with the synthesis of reduced graphene oxide-polypyrrole nanotubes nanocomposites with varying concentration of reduced graphene oxide by an in-situ reduction method. The physico-chemical properties of the constituent components and the nanocomposites have been studied by using different characterization techniques. The electrochemical performance of the nanocomposites has been investigated in terms of parameters such as specific capacitance, coulombic efficiency, energy density, power density and cycle life by cyclic voltammetry and galvanostatic charge-discharge measurements. The equivalent series resistance and charge transfer resistance of the pristine and nanocomposite electrodes across the interface have been evaluated using electrochemical impedance spectroscopy.

4.1 Introduction

Conducting polymers (CPs) such as polypyrrole (PPy), polyaniline (PAni) and polyethylene dioxythiophene (PEDOT) with good electrical conductivity, redox reversibility and large pseudocapacitance have aroused wide interest as electrode materials for supercapacitor applications [261]. The rising interest of CP based materials is stimulated by the demand for high specific capacitance and energy density as well as low fabrication cost. To improve the performances and extend the functions of energy storage devices, CPs are usually nanostructured [262]. The large surface area created by nanoscale structures enhances the efficiency and performance of an electrode material by increasing the electrolyte transport rate and therefore improves the electrode. Among the CPs, PPy is considered to be a highly promising electrode material for energy storage applications owing to its low cost, easy synthesis, high energy storage capacity, environmental stability and relatively high

conductivity [263-265]. However, its practical application is limited by its low power density and poor cycling stability during charging/discharging owing to the easily damaged structure of the material during the redox process [266, 267]. In order to resolve this issue, nanocomposites of CPs with carbon nanotubes, graphene or reduced graphene oxide (RGO), graphene oxide (GO), inorganic materials have been fabricated and improved performance of these nanocomposites as compared to pristine CPs have been achieved [268-271]. Graphene has attracted much attention in energy storage application because of its large specific surface area along with exceptional thermal, mechanical and electrical properties [272]. As an essential characteristic of electrode material, the very large electrochemically active surface area of graphene is the most notable feature, which determines the capacitance [32]. However, large scale production of high quality graphene still remains a challenge using current technologies that include micromechanical cleavage, epitaxial growth on silicon carbide or metal surface and chemical vapor deposition [273]. Therefore, RGO or multilayered graphene derived from the chemical reduction of GO is used as a desirable alternative to pristine graphene due to its easy processing of chemical exfoliation and nearly graphene like properties [274]. However, restacking of RGO especially after chemical reduction reduces its intrinsic capacitance and significantly hampers their performance as electrodes. One of the possible prevention of aggregation of RGO is the use of CP nanostructures as spacers. *In situ* chemical reduction of GO in presence of CP nanostructures can not only restore the conductivity of RGO but can prevent their irreversible restacking also because of the presence of CPs as spacers between them [119]. Furthermore, the synergistic effect of CP nanostructures and RGO may further boost the specific capacitance of the nanocomposites by simultaneously combining the EDL and pseudocapacitive charge storage mechanisms. Compared to other CP nanostructures, 1D nanotubes provide facile ion transport, large aspect ratio and internal hollow structure thereby making both its interior and exterior surface accessible to the electrolyte. CP nanotubes can serve as a spacer to enhance the surface area of RGO, while RGO nanosheets can improve the electrical conductivity and cycling stability of the resultant nanocomposites by providing a stable and underlying conductive network [275].

This chapter deals with nanocomposites of RGO and PPyNTs with varying RGO concentration synthesized by *in situ* reduction of GO in presence of PPyNTs to prevent the restacking of RGO nanosheets. The detailed synthesis procedure and

sample compositions of RGO-PPyNTs nanocomposites have been discussed in section 3.2 of Chapter 3. The morphology, chemical structure and composition of the pristine components and the nanocomposites have been studied by SEM, HRTEM, XRD, FTIR and micro-Raman spectroscopy. Thermal stability, current-voltage characteristics and conductivity of the nanocomposites have been investigated with increasing RGO concentration. The electrochemical performance of the nanocomposites with varying RGO concentration has been investigated by cyclic voltammetry, galvanostatic charge-discharge measurements and electrochemical impedance spectroscopy. The electrochemical stability of the nanocomposites has been tested for 1000 cycles and compared with that of pristine PPyNTs.

4.2 Structural characterization

4.2.1 Morphological analysis

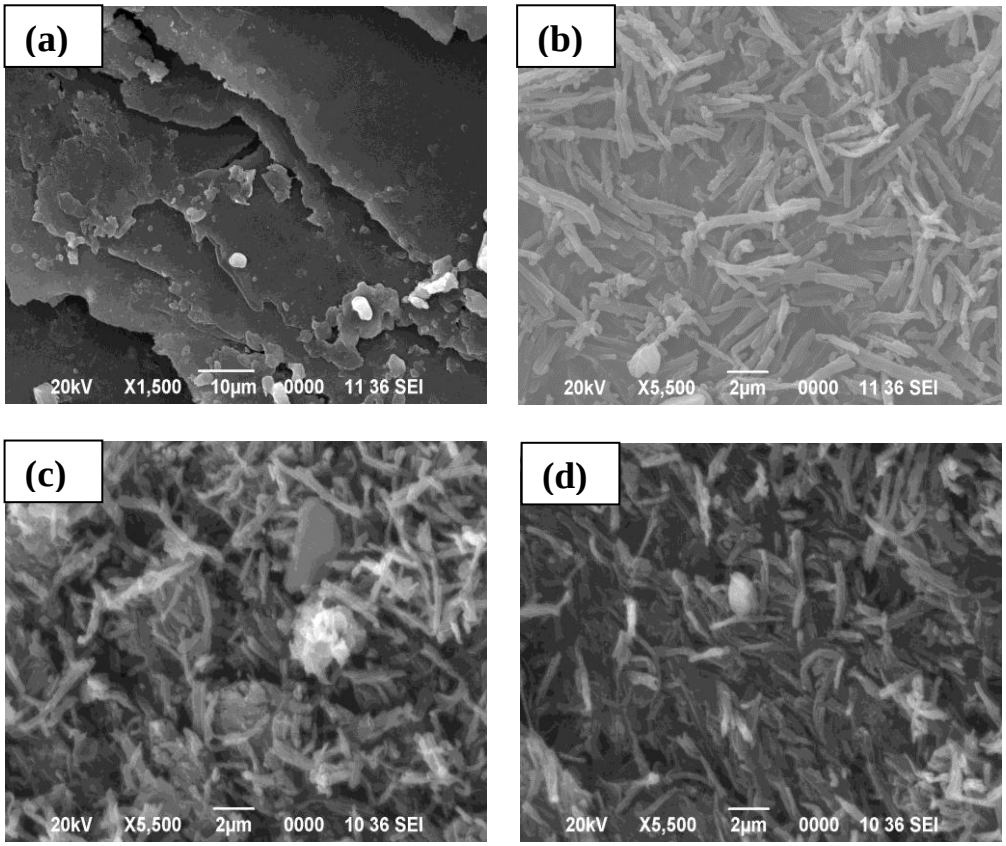

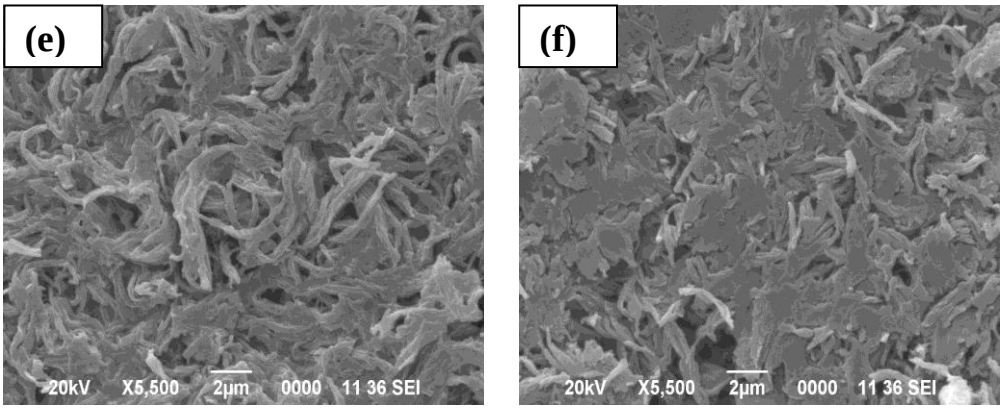

Figure 4.1: *SEM images of (a) RGO, (b) PPyNTs and RGO-PPyNTs nanocomposites with (c) 5 wt. %, (d) 10 wt. %, (e) 20 wt. % and (f) 40 wt. % of RGO.*

The morphological observation of RGO, PPyNTs and nanocomposites were carried out using SEM (Figure 4.1) and HRTEM (Figure 4.2). HRTEM micrograph of RGO (Figure 4.2 (a)) depicts a flat paper-like morphology with wrinkles on the surface indicating that the sheets are very thin. Figure 4.2 (b) demonstrates hollow tubular structure of PPy with an average outer diameter around 132 nm confirming the formation of PPyNTs. From the HRTEM micrograph of the 10 wt. % nanocomposite as depicted in Figure 4.2 (c), it is observed that PPyNTs are well organized on the large surface area of RGO nanosheets. The SEM image of RGO depicts several sheets stacked together in layered form. Figure 4.1 (b) displays randomly oriented PPyNTs having diameter in nano range. In the SEM image of 5 wt. % RGO-PPyNTs nanocomposite, PPyNTs are seen to aggregate due to its higher ratio, but a homogeneous distribution of nanotubes is observed with an increase in the RGO concentration. PPyNTs are observed on the surface of RGO nanosheets, which suggests that PPyNTs act as spacers between RGO nanosheets. As RGO exhibits a negative charge due to the presence of oxygen containing groups in its basal plane and edges, and PPyNTs carries a positive charge on its backbone upon oxidation, so there is electrostatic attraction between the two components in the nanocomposites that self-assembles them together [276]. Such a role of PPyNTs is not only helpful in preventing the restacking of RGO nanosheets after *in situ* reduction but also enhances the surface area of the nanocomposites.

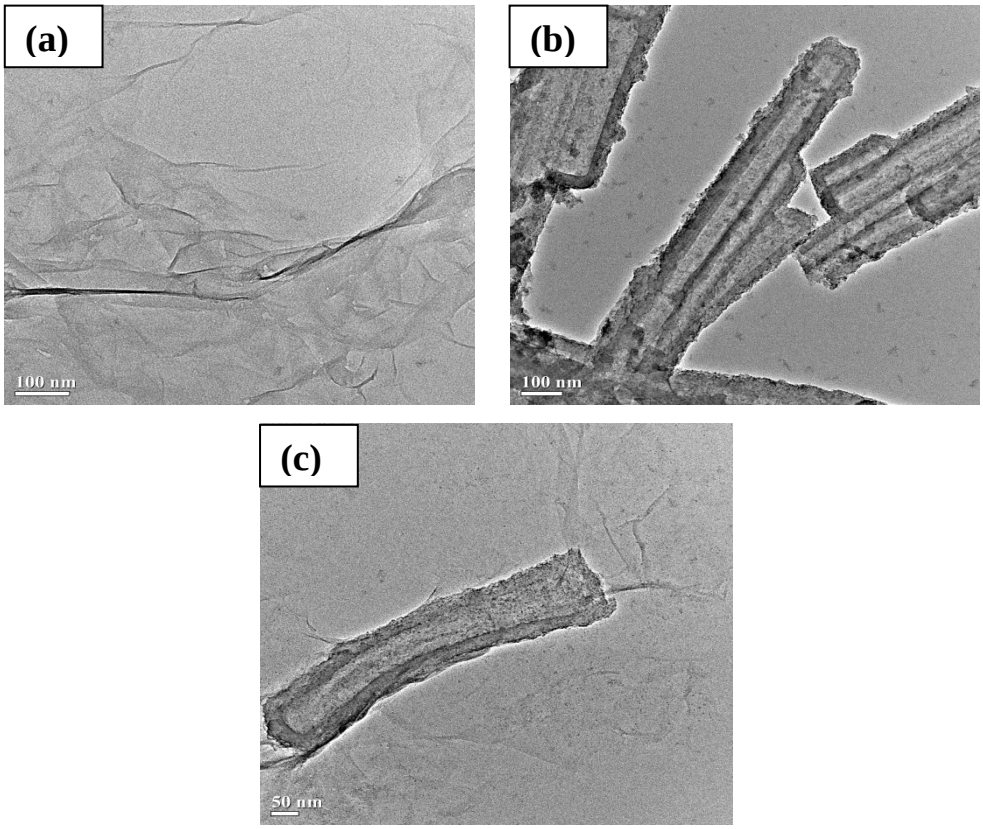

Figure 4.2: *HRTEM micrographs of (a) RGO nanosheets, (b) PPyNTs and (c) 10 wt.% RGO-PPyNTs nanocomposite.*

4.2.2 X-ray diffraction analysis

The XRD patterns of graphite, GO, RGO and PPyNTs are presented in Figure 4.3 (i). Graphite exhibits an intense diffraction (002) peak at $2\theta = 26.6°$ corresponding to an interlayer spacing of 0.33 nm [277]. On chemical oxidation of graphite, the (002) diffraction peak shifts to lower angle at $2\theta = 9.93°$ indicating a larger interlayer spacing of 0.88 nm. The increase in interlayer spacing is due to the incorporation of oxygen functional groups like carboxyl, epoxide, hydroxyl and water molecules into the interlayer galleries of graphite thus supporting the formation of graphite oxide [278]. In the XRD pattern of RGO, the (002) peak of graphite oxide vanishes at 9.93° and appears at $2\theta = 24.6°$, which indicates the loss of long range stacking order and exfoliation of graphite oxide. This gives an interlayer spacing of 0.36 nm which is much smaller than 0.88 nm of that of graphite oxide and is closer to graphite thereby confirming the efficient removal of oxygen functional groups from graphite oxide. Pristine PPyNTs show a broad amorphous peak centered around $2\theta = 20°$-30°, which is attributed to the π-π interaction of partial PPy chains [279]. In the XRD

patterns of RGO-PPyNTs nanocomposites as shown in Figure 4.3 (ii), a broad peak is observed in the range of 19°-30°, which is attributed to overlapping of the reflection peaks of RGO at 24.6° and PPyNTs at 20°-30°. The relative percentage of crystallinity (X_c) of PPyNTs and the nanocomposites has been calculated by measuring the amorphous area and the area under the crystalline peak using equation (3.7). The relative crystallinity values are calculated to be 22, 25, 27, 30 and 33% for PPyNTs and RGO-PPyNTs nanocomposites with 5, 10, 20 and 40 wt. % of RGO, respectively. It is observed that the percentage of crystallinity of the nanocomposites increases with increase in RGO concentration. This is due to the increasing content of crystalline component RGO in the nanocomposites.

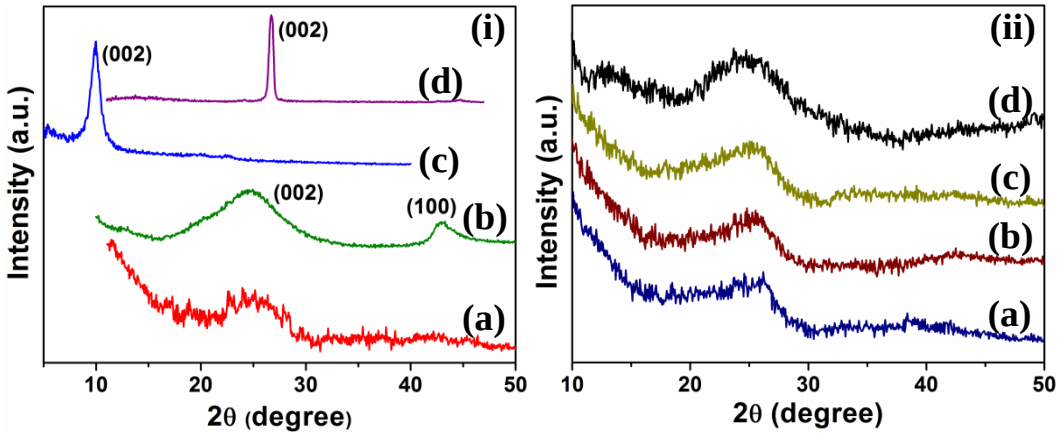

Figure 4.3: *(i) X-ray diffractograms of (a) PPyNTs, (b) RGO, (c) GO and (d) graphite; (ii) XRD patterns of RGO-PPyNTs nanocomposites with (a) 5 wt. %, (b) 10 wt. %, (c) 20 wt. % and (d) 40 wt. % of RGO.*

4.3 Vibrational spectroscopy

4.3.1 Fourier transform infrared spectroscopy

The FTIR spectra of RGO, PPyNTs and RGO-PPyNTs nanocomposites in the range of 400-4000 cm^{-1} are shown in Figure 4.4. The FTIR spectrum of PPyNTs exhibits characteristic absorption bands at 1544 and 1460 cm^{-1} that are assigned to C=C stretching and C-N stretching vibration, respectively [280]. The vibrations observed at 1037 cm^{-1} and 1312 cm^{-1} are attributed to C-H in-plane stretching vibrations of PPyNTs, respectively [281]. The strong bands near 1178 and 903 cm^{-1} indicate the doped states of PPyNTs [282]. The spectrum of RGO shows an absorption band at 1628 cm^{-1} for C=C stretching, indicating the restoration of the graphene network on

reduction [283]. The weak absorption peak of RGO at 1023 cm^{-1} represents C-O stretching vibrations suggesting the presence of residual oxygen groups after reduction [284]. The broad absorption peaks centering at around 3438 and 3416 cm^{-1} for RGO and PPyNTs corresponds to the O-H and N-H stretching vibrations [285, 286] both of which overlaps in the FTIR spectra of the nanocomposites. The 1628 cm^{-1} peak of RGO is observed as a weak shoulder for 40 wt. % RGO-PPyNTs nanocomposite, which is not distinct for 5, 10 and 20 wt. % nanocomposites due to its low content. The signals related to CH and CH_2 stretching appears at 2853 and 2924 cm^{-1} [287] for both PPyNTs and RGO as well as in the nanocomposites. It is observed that the peaks of PPyNTs at 1544, 1460, 1178 and 903 cm^{-1} shift towards higher wave numbers to 1557, 1475, 1197 and 927 cm^{-1}, respectively in the nanocomposites. The shifting is attributed to the π-π interaction between PPy chains and RGO sheets restricting the modes of vibrations of PPy resulting in absorbance at lower wavelength [233]. Table 4.1 presents the IR bands of PPyNTs and RGO along with their respective positions.

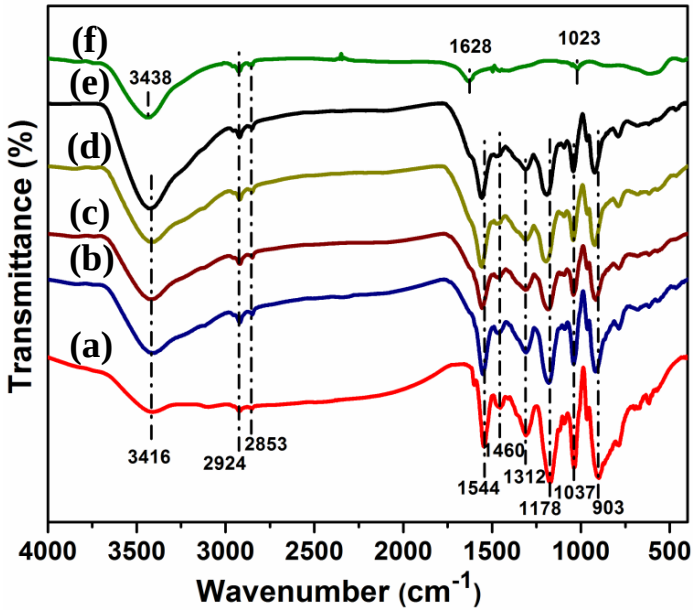

Figure 4.4: *FTIR spectra of (a) PPyNTs and RGO-PPyNTs nanocomposites with (b) 5 wt. %, (c) 10 wt. %, (d) 20 wt. %, (e) 40 wt. % of RGO and (f) RGO.*

Table 4.1: *Characteristic IR bands of PPyNTs, RGO and their assignments*

IR Bands	**Assignments**
PPyNTs	
903, 1178 cm^{-1}	Doped states of PPyNTs [282]
1037, 1312 cm^{-1}	C-H in-plane stretching [281]
1460 cm^{-1}	C-N stretching [280]
1544 cm^{-1}	C=C stretching [280]
2853, 2924 cm^{-1}	CH and CH_2 stretching [287]
3416 cm^{-1}	N-H stretching [286]
RGO	
1023 cm^{-1}	C-O stretching [284]
1628 cm^{-1}	C=C stretching [283]
2853, 2924 cm^{-1}	CH and CH_2 stretching [287]
3438 cm^{-1}	O-H stretching [285]

4.3.2 Micro-Raman spectroscopy

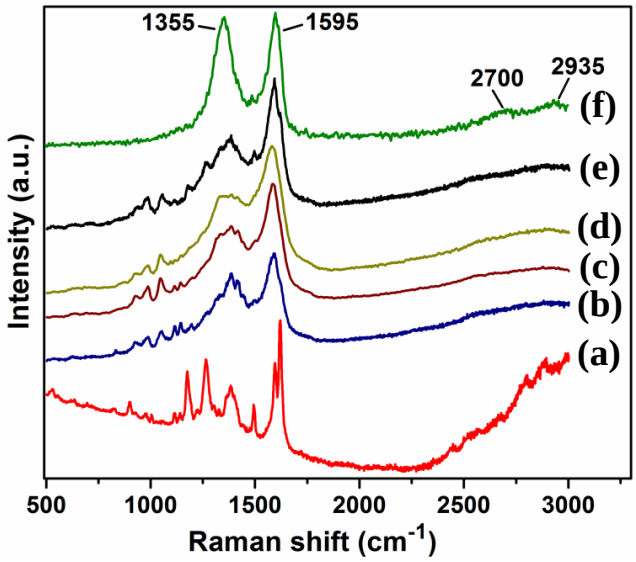

Figure 4.5: *Micro-Raman spectra of (a) PPyNTs and RGO-PPyNTs nanocomposites with (b) 5 wt. %, (c) 10 wt. %, (d) 20 wt. %, (e) 40 wt. % of RGO and (f) RGO.*

The significant structural changes of the nanocomposites have been investigated by micro-Raman spectroscopy in the range of 500-3000 cm^{-1} and are displayed in Figure 4.5. The μ-Raman spectrum of RGO exhibits two prominent bands: D and G

bands at 1355 cm^{-1} and 1595 cm^{-1}, respectively. The D band known as the disorder or the defect band represents a breathing mode from sp^2 carbon rings caused by the first-order zone boundary phonons and requires a defect for its activation [288]. The G band arises due to the in-plane optical vibrational mode of two neighbouring carbon atoms on a sp^2-hybridized RGO layer [289]. The appearance of the D band in the RGO spectrum indicates the presence of structural defects and partially disordered structures formed during the chemical synthesis of RGO [290]. A band appearing at 2700 cm^{-1} known as 2D band corresponds to in-plane breathing mode of carbon rings of RGO [291]. In addition, the band at 2935 cm^{-1} in the Raman spectra of RGO represents the DG combination band [208]. The broad 2D band is a signature of a multilayered structure of RGO. The Raman spectra of PPyNTs include the peaks at 930 cm^{-1}, 982 cm^{-1}, 1265 cm^{-1}, 1382 cm^{-1} and 1588 cm^{-1}. The characteristic bands at 1588 and 1382 cm^{-1} are attributed to the stretching of the π conjugated structure and the ring stretching mode of PPyNTs, respectively [292]. These characteristic peaks of PPyNTs are found to overlap with the D and G bands of RGO in the Raman spectra of the nanocomposites. The band at 1265 cm^{-1} appearing for PPyNTs is assigned to the C-H in-plane stretching vibration [293]. The small peaks at 930 and 982 cm^{-1} are associated with ring deformation of dication and radical cation, respectively, which justify the doped state of PPy [294]. The micro-Raman spectra of the nanocomposites exhibit peaks at 922, 982, 1355 and 1595 cm^{-1}, which reveals the co-existence of RGO and PPyNTs. The characteristic micro-Raman peaks of PPyNTs and RGO with their corresponding peak positions have been assigned in Table 4.2.

Table 4.2: *Characteristic micro-Raman bands of PPyNTs, RGO and their assignments*

Raman Bands	**Assignments**
PPyNTs	
930 cm^{-1}	Ring deformation associated with dication [294]
982 cm^{-1}	Ring deformation associated with radical cation [294]
1265 cm^{-1}	C-H in-plane stretching [293]
1382 cm^{-1}	Ring stretching mode [292]
1588 cm^{-1}	Stretching of π conjugated structure [292]

RGO	
1355 cm^{-1}	D band: breathing mode from sp^2 carbon rings [288]
1595 cm^{-1}	G band: in-plane sp^2 C-C stretching [289]
2700 cm^{-1}	2D band: in-plane breathing mode of carbon rings [291]
2935 cm^{-1}	DG combination band [208]

4.4 Thermogravimetric analysis

The thermal stability of PPyNTs, RGO and RGO-PPyNTs nanocomposites has been investigated within the temperature range of 50-700 ºC. The thermogravimetric (TG) curves of the samples have been individually depicted in Figure 4.6. The thermal degradation patterns of pristine components and nanocomposites are a two-step degradation process. The first degradation is observed below 100 ºC for all samples, which is attributed to the loss of residual moisture. RGO exhibits a slow degradation due to evaporation of residual oxygen functional groups such as –OH, –CO–, and –COOH groups in its structure, but exhibits very good thermal stability having only 26.1% degradation up to 700 ºC [295]. In contrast to this, PPyNTs exhibit a sharp degradation starting at 242 ºC corresponding to the decomposition of PPy backbone and degrades 93.5% upto 700 °C [278]. It is clearly observed from the TG curves that increase in RGO concentration in the nanocomposites leads to an increase in the second degradation temperature indicating the superior thermal stability of the nanocomposites than that of pristine PPyNTs. This superior thermal stability of the nanocomposites is attributed to the increased crystallinity of the nanocomposites with increase in RGO loading as confirmed from XRD analysis.

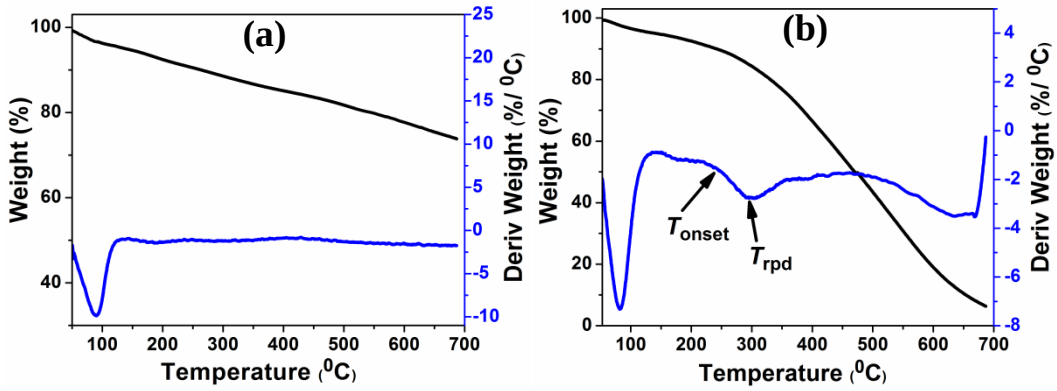

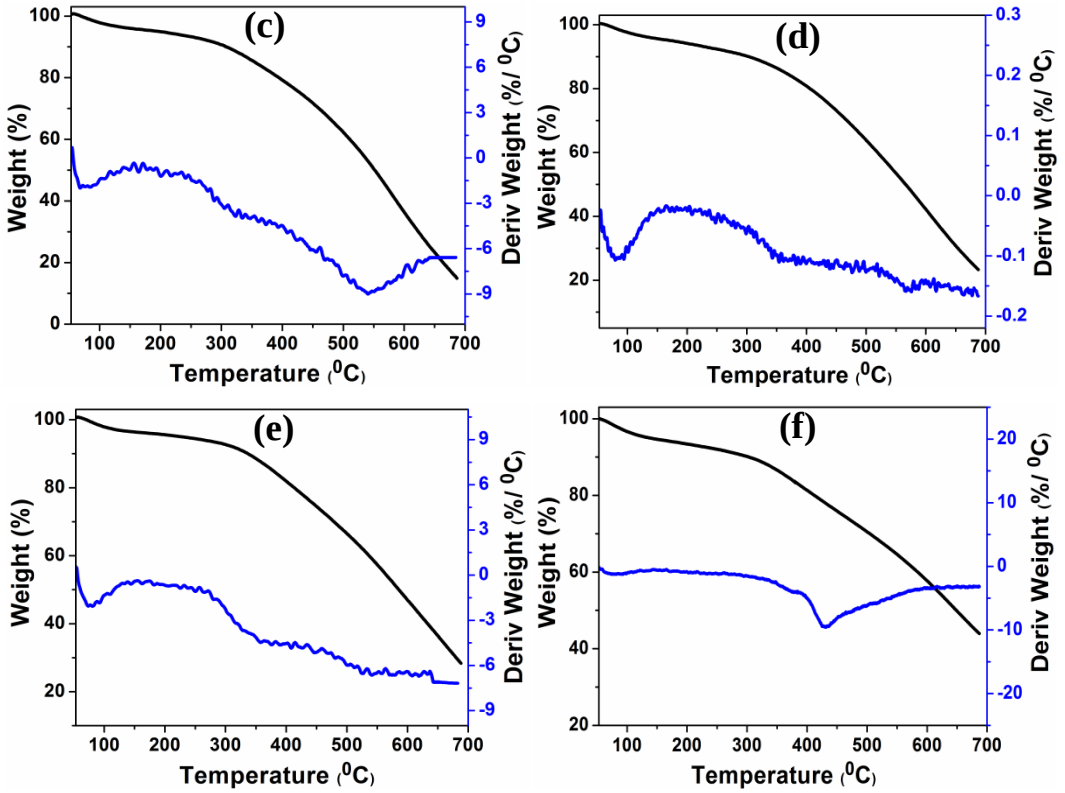

Figure 4.6: *TG and derivative of TG curves of (a) RGO, (b) PPyNTs and RGO-PPyNTs nanocomposites with (c) 5 wt. %, (d) 10 wt. %, (e) 20 wt. % and (f) 40 wt. % of RGO.*

The onset decomposition (T_{onset}) and rapidest decomposition (T_{rpd}) temperatures of RGO, PPyNTs and RGO-PPyNTs nanocomposites have been measured from the derivative plots of TG curves. The derivative TG plots are shown in blue in Figure 4.6 and the measured values of T_{onset} (temperature at which degradation starts) and T_{rpd} (temperature at which degradation rate is maximum) for the second degradation mechanism are summarized in Table 4.3. RGO does not exhibit onset and rapidest decomposition temperatures as it does not show a sharp second degradation within the temperature range of 50-700 ºC. For PPyNTs and the nanocomposites, the TG derivative curves exhibit two peaks that correspond to two different degradation mechanisms of residual water and the polymer chain, respectively. It is observed that with increasing concentration of RGO, T_{onset} and T_{rpd} of the nanocomposites increases attaining the highest values of T_{onset} = 304 ºC and T_{rpd} = 429 ºC for 40 wt. % of RGO concentration. In contrast to this, PPyNTs exhibit T_{onset} = 242 °C and T_{rpd} = 300 °C which is lower than that of the nanocomposites, indicating the fast degradation of the polymer chain in the absence of RGO. This

shows that thermal stability of the nanocomposite system is enhanced with increase in RGO loading. This could be attributed to stabilization of the thermally degraded component of PPyNTs by RGO, which acts as a mass transport barrier to the volatile components of PPy giving rise to higher degradation temperature of the nanocomposites.

Table 4.3: *T_{onset}, T_{rpd} and % of degradation at 700 °C of RGO, PPyNTs and RGO-PPyNTs nanocomposites*

Sample	T_{onset} (°C)	T_{rpd} (°C)	Degradation at 700 °C (%)
RGO	–	–	26.1
PPyNTs	242	300	93.5
5 wt. % RGO	276	352	84.9
10 wt. % RGO	288	360	76.3
20 wt. % RGO	290	379	69.8
40 wt. % RGO	304	429	55.7

4.5 Current-voltage (I-V) characteristics

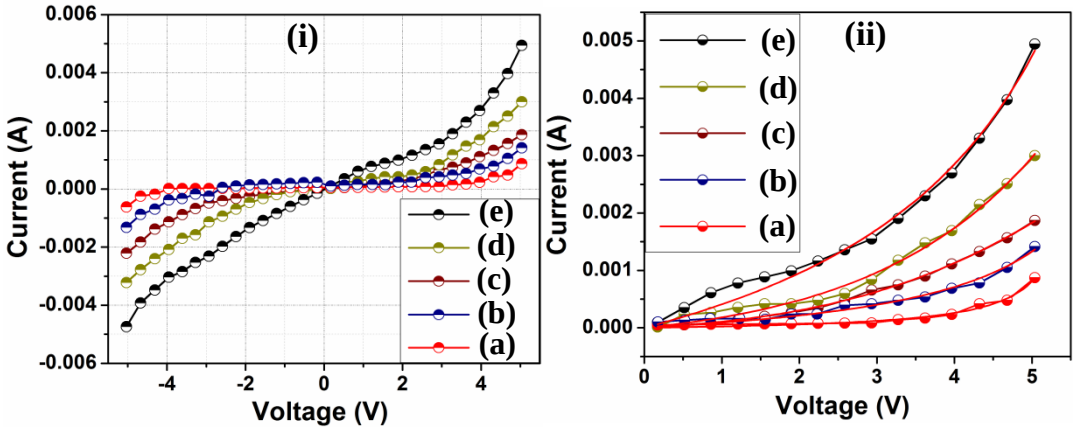

Figure 4.7: *(i) I-V characteristics and (ii) Kaiser equation fitted positive sides of I-V characteristic curves of (a) PPyNTs and RGO-PPyNTs nanocomposites with (b) 5 wt. %, (c) 10 wt. %, (d) 20 wt. % and (e) 40 wt. % of RGO.*

The I-V characteristics of PPyNTs and RGO-PPyNTs nanocomposites have been carried out using a two-probe unit at room temperature and presented in Figure 4.7 (i). From the plot, it is observed that the I-V characteristics of pristine PPyNTs and

the nanocomposites are non-linear and symmetric in nature. The non-linear I-V characteristic of PPyNTs is a result of its non-homogeneous structure, having ordered chain foldings (metallic regions) in its structure that are separated by disordered dielectric barriers [296]. The nanocomposites also exhibit non-linear I-V characteristics, which is attributed to their inhomogeneous structure due to dispersion of highly conductive RGO nanosheets in relatively less conducting PPyNTs matrix. In order to understand the non-linear behavior of I-V characteristics in a quantitative manner, we have used the model proposed by Kaiser et al. given by equation (2.24). We note that all these I-V characteristics are essentially symmetric upon reversal of the voltage direction, so only the positive sides of I-V characteristics are fitted according to equation (2.24) and the fitted curves are presented in red solid lines in Figure 4.7 (ii). The parameters obtained from the fitted curves are listed in Table 4.4. It is observed that the fitting parameters namely, low field conductance (G_0), voltage scale factor (V_0) and h exhibit higher values on increasing the concentration of RGO in RGO-PPyNTs nanocomposites. The increase in V_0 with increasing RGO concentration indicates decreased non-linearity of the I-V curves. Also, an increase in the value of h from 0.65 (PPyNTs) to 0.90 (40 wt. % of RGO) is noticed which corresponds to the increase in conductance at low field.

Table 4.4: *Fitting parameters to Kaiser equation for PPyNTs and RGO-PPyNTs nanocomposites with different RGO concentrations*

Sample	G_0**(S)**	V_0 **(V)**	h
PPyNTs	1.23×10^{-4}	1.55	0.65
5 wt. % RGO	2.62×10^{-4}	1.87	0.72
10 wt. % RGO	4.3×10^{-4}	2.45	0.80
20 wt. % RGO	6.3×10^{-4}	2.72	0.82
40 wt. % RGO	9.4×10^{-4}	3.12	0.90

4.6 Conductivity measurements

Electrical conductivity of RGO, PPyNTs and RGO-PPyNTs nanocomposites has been calculated using equation (2.26). The measured value of conductivity of pure PPyNTs is 0.34 S cm^{-1} and that of pure RGO is 9.21 S cm^{-1}. The conductivity of RGO-PPyNTs nanocomposites with 5, 10, 20 and 40 wt. % loading of RGO is

measured to be 1.31, 1.94, 2.76 and 4.47 S cm^{-1}, respectively as compared to pure PPyNTs. An increase in conductivity of the nanocomposites is observed with increase in RGO concentration, which can be attributed to the formation of connected network of conducting RGO in less conducting PPyNTs matrix [297]. RGO nanosheets act as "conduction link" between PPyNTs providing a small resistance path for charge transfer [298]. Moreover, the high aspect ratio of RGO nanosheets with 1D structure of PPyNTs facilitates the electron transfer process in the nanocomposites.

4.7 Electrochemical properties

4.7.1 Cyclic voltammetry

The CV measurements of PPyNTs and RGO-PPyNTs nanocomposites have been conducted at different scan rates in 1 M KCl electrolyte within the potential range of -0.2 V to 0.8 V and are shown in Figure 4.8. PPyNTs exhibit a non-rectangular CV curve indicating pseudocapacitive charge storage mechanism. The CV curve of the nanocomposites indicates an enhanced current response and larger enclosed area with increase in RGO concentration implying improved charge storage behavior. Moreover, a transition in the shape of the CV curves from non-rectangular to rectangular shape is observed with increase in RGO concentration. This transition is due to the increased EDL capacitance of the nanocomposite electrodes with increase in RGO loading. The nanocomposite with 40 wt. % of RGO displays a quasi-rectangular CV shape with a slight distortion, which implies the combination of both EDL and pseudocapacitive charge storage processes in the electrode.

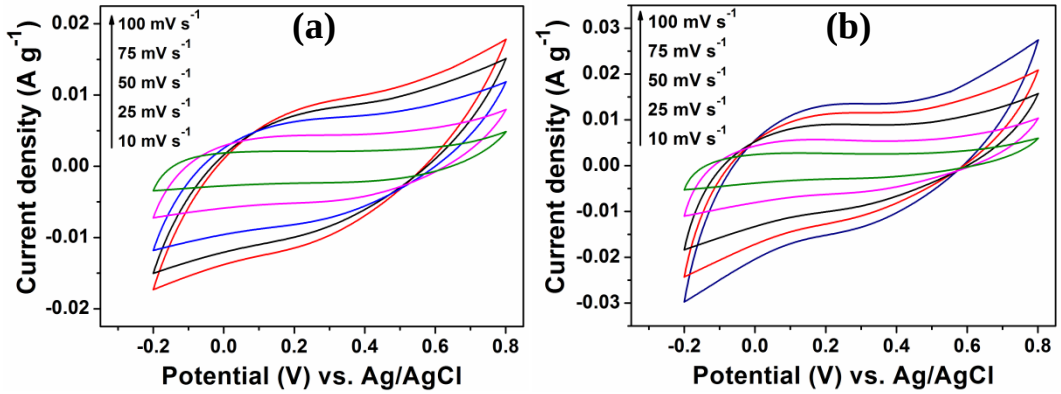

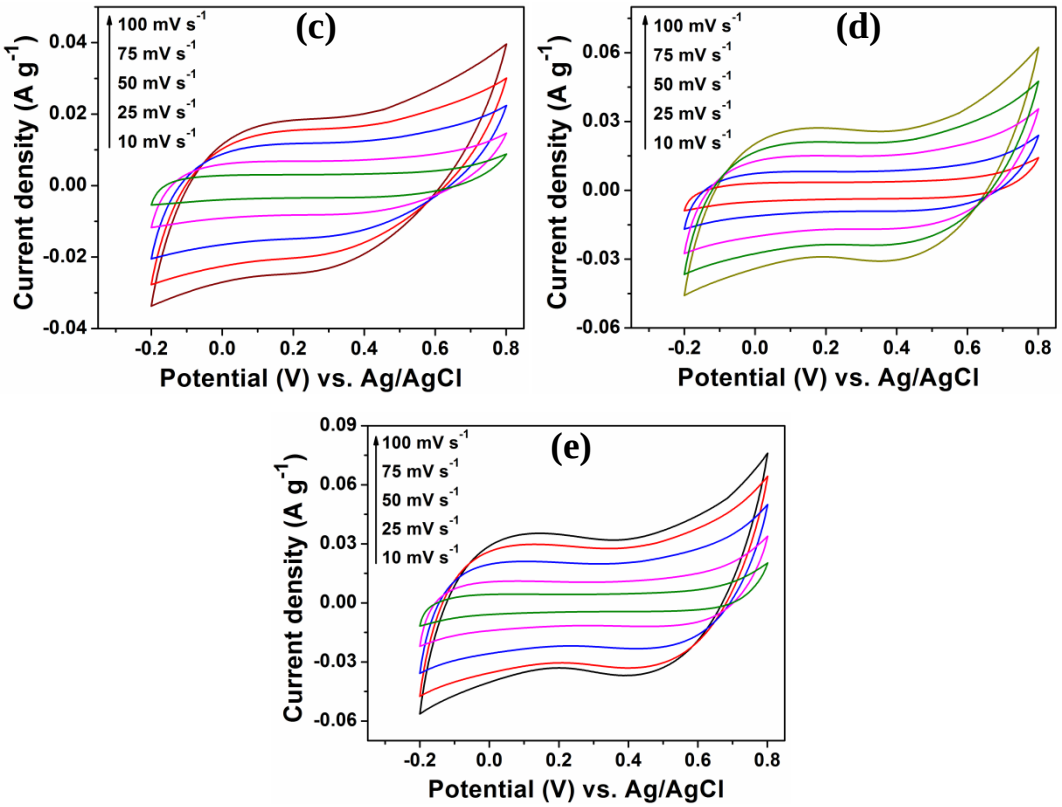

Figure 4.8: *CV curves at different voltage scan rate of (a) PPyNTs and RGO-PPyNTs nanocomposites with (b) 5 wt. %, (c) 10 wt. %, (d) 20 wt. % and (e) 40 wt. % of RGO.*

4.7.2 Galvanostatic charge-discharge measurements

The galvanostatic charge-discharge measurements of PPyNTs and RGO-PPyNTs nanocomposites performed between 0 and 0.8 V at a current density of 0.5 A g^{-1} are shown in Figure 4.9 (i). It is observed that PPyNTs exhibits a non-linear discharge due to its pseudocapacitive charge storage process. Upon incorporation of RGO, the discharge curves are observed to be symmetric and linear indicating improved capacitive behavior. For the nanocomposite with 20 and 40 wt. % of RGO, the charge-discharge curves are almost symmetric with a slight curvature, which arises due to the EDL contribution of RGO along with the pseudocapacitive contribution of PPyNTs. The discharge time of the nanocomposites is substantially prolonged as compared to pristine PPyNTs, which indicates increased specific capacitance. The longest duration is obtained for 40 wt. % of RGO, which exhibits the highest specific capacitance. Also, a significant decrease in internal resistance (IR drop) of the nanocomposites has been observed with increase in RGO loading.

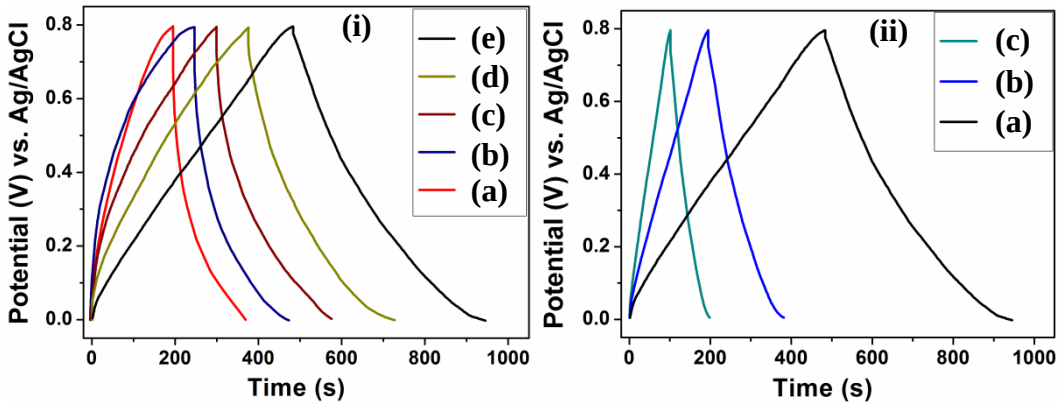

Figure 4.9: *(i) GCD curves of (a) PPyNTs and RGO-PPyNTs nanocomposites with (b) 5 wt. %, (c) 10 wt. %, (d) 20 wt. % and (e) 40 wt. % of RGO at a current density of 0.5 A g^{-1}; (ii) GCD curves of 40 wt. % RGO-PPyNTs nanocomposite at a current density of (a) 0.5 A g^{-1}, (b) 1 A g^{-1} and (c) 1.5 A g^{-1}.*

The specific capacitance (C_{sp}) and coulombic efficiency (η) have been evaluated from the GCD curves using the following equations:

$$C_{sp} = \frac{I\Delta t_d}{m\Delta V} \tag{4.1}$$

$$\eta = \frac{\Delta t_d}{\Delta t_c} \times 100\% \tag{4.2}$$

where m is the mass of the electrode material, I is the applied constant current, ΔV is the discharge potential and Δt_d and Δt_c are the discharging and the charging times, respectively. The calculated values of specific capacitance and coulombic efficiency are listed in Table 4.5. A maximum specific capacitance of 299.81 F g^{-1} and coulombic efficiency of 96% is obtained for the nanocomposite with 40 wt. % of RGO. The higher coulombic efficiency of the nanocomposites as compared to pristine PPyNTs is due to the increasing linear shape of the charge and discharge curves with enhanced RGO loading. The GCD curves of 40 wt. % RGO-PPyNTs nanocomposite at different current densities are presented in Figure 4.9 (ii). The extended discharge duration of the nanocomposites may be attributed to the combined double-layer and pseudocapacitive contribution to the total capacitance, while the short discharge duration in PPyNTs indicates the pseudocapacitive nature of the fabricated electrode [299]. Thus a synergistic effect is observed in the nanocomposite system. The enhanced electrochemical behavior of the nanocomposites is attributed to the nanoscale structure of RGO and PPyNTs which

ensures the following advantages to its functions: (i) the highly conductive RGO can provide a easy pathway for the transportation of ions and electrons, which in turn reduces the internal resistance of the nanocomposites, (ii) PPyNTs can act as a spacer that prevents the aggregation of RGO nanosheets resulting in an enhanced EDL contribution, and (iii) the high surface area of RGO nanosheets increases the contact area between the electrode and electrolyte. The energy density and power density values have been calculated from the GCD curves using equations (2.30) and (2.31), respectively and are presented in Table 4.5. A high energy density of 24 W h kg^{-1} and power density of 192 W kg^{-1} is obtained for 40 wt. % RGO-PPyNTs nanocomposite.

Table 4.5: *Specific capacitance, energy density, power density, coulombic efficiency, equivalent series resistance (R_s) and charge transfer resistance (R_{ct}) of PPyNTs and RGO-PPyNTs nanocomposites*

Sample	**Specific capacitance ($F\ g^{-1}$)**	**Energy density ($W\ h\ kg^{-1}$)**	**Power density ($W\ kg^{-1}$)**	**Coulombic efficiency**	**R_s (Ω)**	**R_{ct} (Ω)**
PPyNTs	128.02	8.22	170.02	89%	12.51	37.45
5 wt. % RGO	164.39	10.87	172.48	92%	12.26	25.58
10 wt. % RGO	197.09	13.79	177.37	93%	9.81	19.23
20 wt. % RGO	238.73	18.15	184.99	94%	8.22	12.02
40 wt. % RGO	299.81	24.68	192.49	96%	6.95	4.6

4.7.3 Electrochemical impedance spectroscopy

The impedance data are analyzed using Nyquist plots and are shown in Figure 4.10 (i) and 4.10 (ii) (magnified view). The equivalent circuit corresponding to the Nyquist plot is presented in the inset of Figure 4.10 (i), which consists of equivalent series resistance (R_s), charge transfer resistance (R_{ct}), the constant-phase element (CPE), the Warburg impedance (Z_w) and the supercapacitor cell capacitance ($C(\omega)$), respectively. R_s is the combined resistance that includes the ionic resistance of the electrolyte, the intrinsic resistance of the active material and the contact resistance at the interface active material [227]. R_{ct} is the charge transfer resistance at the electrode/electrolyte interface.

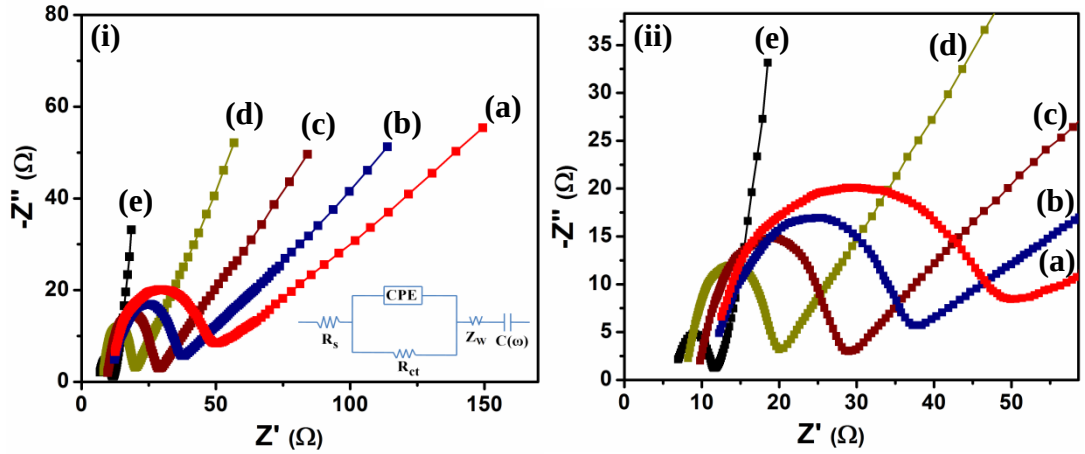

Figure 4.10: *(i) Nyquist plots of (a) PPyNTs and RGO-PPyNTs nanocomposites with (b) 5 wt. %, (c) 10 wt. %, (d) 20 wt. % and (e) 40 wt. % of RGO (Inset shows equivalent circuit) and (ii) Magnified view of the Nyquist plot in Z' range of 0 to 60 Ω.*

All the Nyquist plots exhibit a semicircle in the high-frequency region and a straight line in the low-frequency region, where the high frequency semicircle intercepts the real axis at R_s and (R_s + R_{ct}) respectively. The high frequency semicircle represents the charge transfer resistance associated with the faradaic reactions and the double-layer capacitance on the electrode surface, while the straight line is determined by ion diffusion [300]. The values of R_s and R_{ct} of PPyNTs and the nanocomposites obtained from the Nyquist plot are depicted in Table 4.5. From the small intercepts, it is evident that R_s is low for all the nanocomposites than that of PPyNTs. The difference in R_s value between PPyNTs and 40 wt. % RGO-PPyNTs being about 5.56 Ω, it appears that high conductivity of the nanocomposite due to the presence of RGO is contributing to the low R_s of the electrode. This clearly demonstrates the reduced interfacial contact resistance between the RGO nanosheets and PPyNTs inside the electrode material. The value of R_{ct} also decreases in the nanocomposites and the lowest value is obtained to be 4.6 Ω for 40 wt. % RGO-PPyNTs nanocomposite. The decreased R_{ct} is ascribed to the high ionic conductivity at the electrode/electrolyte interface [301]. The slope of the 45° portion of the curve in the Nyquist plot is a signature of Warburg impedance, which is representative of ion diffusion/transport from the electrolyte to the electrode surface [302]. The Warburg resistance is reduced in the nanocomposites, which indicates short ion diffusion path lengths and decreased obstruction of ion movement to and within the electrode

[303]. Moreover, a vertical shape at lower frequencies in the Nyquist plot implies ideal capacitive behavior [113], which is observed for 40 wt. % of RGO incorporated PPyNTs nanocomposite electrode.

4.7.4 Cyclic stability study

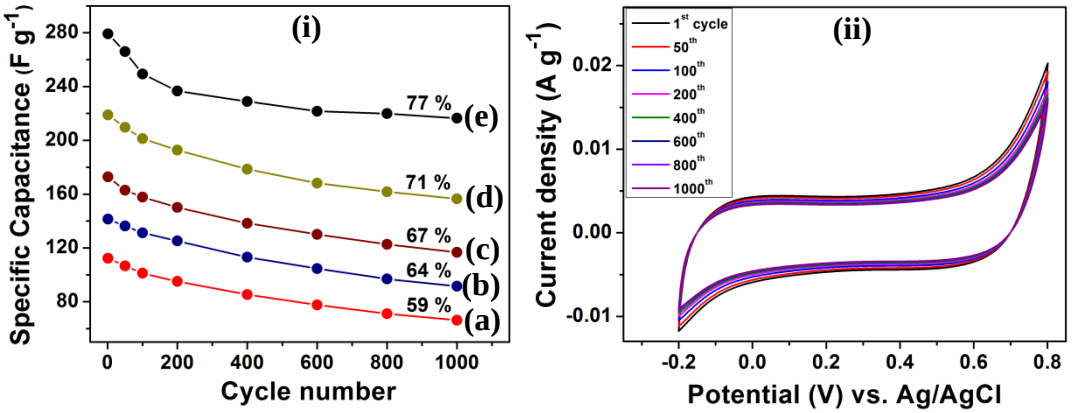

Figure 4.11: *(i) Variation of specific capacitance with cycle number of (a) PPyNTs and RGO-PPyNTs nanocomposites with (b) 5 wt. %, (c) 10 wt. %, (d) 20 wt. % and (e) 40 wt. % of RGO; (ii) CV curves with increasing cycle number of 40 wt. % RGO-PPyNTs nanocomposite.*

The electrochemical stability of PPyNTs and RGO-PPyNTs nanocomposites has been investigated by repeating the CV measurements in 1 M KCl electrolyte at a scan rate of 10 mV s^{-1} for 1000 cycles. The specific capacitance (C_{sp}) values with increasing number of CV cycles for PPyNTs and the nanocomposites have been calculated using the equation:

$$C_{sp} = \frac{1}{2}\left(\frac{\int_{V_1}^{V_2} I(V)dV}{mv\Delta V}\right) \tag{4.3}$$

where m is the mass of the electrode material, $\int_{V_1}^{V_2} I(V)dV$ is the enclosed CV area, v is the potential scan rate and ΔV is the potential window range. The plot of specific capacitance with cycle number is presented in Figure 4.11 (i). It is observed that about 59% of the initial specific capacitance has been retained by PPyNTs electrode after 1000 cycles. The cyclic stability of the nanocomposites increases with increasing RGO concentration and a maximum capacitive retention of 77% after 1000 cycles is achieved for the nanocomposite electrode with 40 wt. % of RGO. The

CV curves of 40 wt. % nanocomposite electrode with increasing cycle number are shown in Figure 4.11 (ii). From the figure, it is seen that the difference between the 1st cycle and the 1000th cycle of 40 wt. % nanocomposite is negligible, suggesting good cyclic stability of the electrode. The discrepancy in electrochemical stability between PPyNTs and 40 wt. % RGO-PPyNTs nanocomposite electrodes may be attributed to the synergistic effect of double-layer and pseudocapacitive contributions in the nanocomposite electrode. While the electrolyte ionic accessibility in the nanocomposite electrode is highly favorable from the hollow structured network of PPyNTs, it appears that the presence of multilayered RGO nanosheets with one dimensional PPyNTs can easily adapt to the volume change experienced by PPy during the charge transfer reactions. Hence a more stable capacitance with good electrochemical stability could be obtained for the nanocomposites as compared to that for PPyNTs.

4.8 Summary

In summary, RGO-PPyNTs nanocomposites with varying RGO concentration have been synthesized by *in situ* reduction of GO in presence of PPyNTs. HRTEM micrographs depict a paper-like morphology of RGO and an average outer diameter of 132 nm is measured for PPyNTs. SEM images display PPyNTs onto the surface of RGO nanosheets, which suggests that PPyNTs act as spacers and prevent the agglomeration of RGO nanosheets. X-ray diffraction analysis indicates the formation of the nanocomposites as the XRD patterns exhibit the diffraction peaks of both RGO and PPyNTs. The broad peak around 19°-30° in the nanocomposites is attributed to overlapping of the reflection peaks of RGO and PPyNTs. An increase in crystallinity from 22% for PPyNTs to 33% for the nanocomposites is obtained with increasing RGO concentration. In the FTIR spectra, a shifting of peaks corresponding to 1544, 1460, 1178 and 903 cm^{-1} of PPyNTs occurs towards higher wave numbers to 1557, 1475, 1197 and 927 cm^{-1}, respectively in the nanocomposites, which is attributed to the π-π interaction between PPy chains and RGO sheets restricting the modes of vibrations of PPy resulting in absorbance at lower wavelength. The micro-Raman spectra of the nanocomposites exhibit two prominent bands of RGO, viz. D and G bands at 1355 cm^{-1} and 1595 cm^{-1}, respectively. The appearance of the D band implies the presence of structural

defects, while the G band arises due to in-plane optical vibrational mode of neighbouring sp^2 bonded carbon atoms. Thermogravimetric analysis reveals that the nanocomposites exhibit a higher degradation temperature of 304 °C than that of 242 °C for pristine PPyNTs. This indicates that the thermal stability of the nanocomposites is enhanced upon incorporation of RGO. The enhanced thermal stability is also corroborated from the higher onset and rapidest decomposition temperatures of the nanocomposites obtained from the derivative TG curves. This is ascribed to stabilization of the thermally degraded component of PPyNTs by RGO, which acts as a mass transport barrier to the volatile components of PPy resulting in slow degradation of the nanocomposites. The I-V curves are symmetric and non-linear in nature, which are well fitted to the Kaiser equation. The fitted curves display higher values of low field conductance (G_0), voltage scale factor (V_0) and h with increasing RGO concentration in the nanocomposites, which indicate decreased non-linearity of the I-V curves. Increase in conductivity of the nanocomposites is achieved with increasing RGO loading, which is due to the presence of RGO nanosheets acting as a "conduction link" between PPyNTs providing a small resistance path for intertube charge transfer. CV studies reveal an enhanced current response and larger enclosed CV area of the nanocomposites as compared to pristine PPyNTs. The CV curve of PPyNTs displays a non-rectangular shape, which is indicative of pseudocapacitive charge storage process. Upon incorporation of RGO, a transition in the CV curve is observed from non-rectangular to nearly rectangular shape, which is ascribed to the increasing contribution of EDLC from RGO in the nanocomposite electrode. The nanocomposite with 40 wt. % of RGO exhibits a quasi-rectangular CV due to the contribution of both EDLC and pseudocapacitance in the electrode. GCD measurements reveal that the nanocomposites exhibit a longer discharge duration as compared to that for PPyNTs, which implies improved capacitive charge storage of the nanocomposites. A maximum specific capacitance of 299 F g^{-1} along with a coulombic efficiency of 96% is obtained from the GCD curves for 40 wt. % RGO-PPyNTs nanocomposite. The nanocomposite with 40 wt. % of RGO exhibits high energy density and power density values of 24 W h kg^{-1} and 192 W kg^{-1}, respectively. EIS studies depict an easier charge transfer and short ion diffusion path length in the nanocomposites after incorporation of RGO. The lowest R_s and R_{ct} values are found to be 6.95 Ω and 4.6 Ω, respectively for the nanocomposite having 40 wt. % of RGO. The cyclic stability of PPyNTs electrode

after 1000 cycles is achieved to be 59%, which is improved to 77% for 40 wt. % RGO-PPyNTs nanocomposite electrode.